Journal of Alloys and Compounds 489 (2010) 700–707

Contents lists available at ScienceDirect

Journal of Alloys and Compounds

journal homepage: www.elsevier.com/locate/jallcom

Synthesis, characterization, and electrical studies on Cu-doped $K_2Ti_6O_{13}$ lead-free ceramics: Role of defect associate dipoles

Satyendra V. Vikram[a,*], D.M. Phase[b], Vishal S. Chandel[a]

[a] *Department of Physics, Integral University, Kursi Road, Lucknow 226026, UP, India*
[b] *UGC–DAE Consortium for Scientific Research, Khandwa Road, Indore 452001, MP, India*

ARTICLE INFO

Article history:
Received 12 September 2009
Accepted 26 September 2009
Available online 9 October 2009

Keywords:
Ceramics
Dielectric response
Phase transitions
X-ray diffraction
Electron paramagnetic resonance

ABSTRACT

Pure and some copper doped ($x = 0.01$, 0.05, 0.1) ceramic specimens of $K_2Ti_6O_{13}$ were synthesised using solid-state route. Lattice constants determined from room temperature XRD data revealed its single phase formation in a monoclinic symmetry. X-band EPR-data, recorded at RT, revealed the substitution of Ti^{4+} lattice sites by two different copper species corresponding to their distinct locally distorted environments. Dielectric data revealed the role of $(Fe'_{Ti}–V_O^{\bullet\bullet})$ *defect associate dipoles* identified as low-field signals ($g \sim 5.43$) in the EPR-spectra on the *ferroelectric–paraelectric* type phase transitions recognized in the $\varepsilon_r(T)$ plots for all the compositions with distinct T_C. Dielectric loss mechanism included space charge polarization, dipole orientation, and electrical conduction. Structural configuration was found to favour polaron conduction and impede the intratunnel ionic conduction. Moreover, electron-hopping conduction was dominant in the low-temperate region whereas intratunnel ionic conduction prevailed at higher temperatures.

1. Introduction

Anderson–Wadsley type alkali titanates, denoted by $A_2O \times nTiO_2$ (A = Li, Na, K), with exclusive layered ($3 \le n \le 5$) and tunnel ($6 \le n \le 8$) crystal structures have been synthesised and characterized using diverse routes [1,2]. Layered $K_{2-x}Na_xTi_4O_9$ and $Na_{2-x}K_xTi_3O_7$ ceramics with various combinations have shown *ferroelectric–ferroelectric* and *ferroelectric–paraelectric* phase transitions [3–5]. While cation exchange property permits some of alkali titanates to protect environment from the lethal radiation of highly radioactive liquid wastes [6], the photocatalytic behaviour of $A_mM_{2n}O_{4n+1}$ ($m = 2, n = 3$) has been interesting [7]. $K_2Ti_6O_{13}$-*whisker* has excellent mechanical properties, good biological features, and similar expansion coefficient to conventional Ti-alloys [8]. Photoreduction of CO_2 with H_2O over $K_2Ti_6O_{13}$ photocatalyst combined with Cu/ZnO catalyst under concentrated sunlight [9]. Titanate whiskers have been shown to have high chemical and thermal stability and potential applications in whisker-reinforced plastics and metals. $K_2Ti_nO_{2n+1}$, with $3 < n < 6$, have a wide band gap of about 3.45 eV while that of TiO_2 is 3.22 eV and thus $K_2Ti_6O_{13}$ is a semiconductive known for its catalytic activity [10].

Moreover, the formation of $K_2Ti_6O_{13}$ nanowires *via* ion exchange for biomedical applications [11] and, structure, growth and optical properties of $K_2Ti_6O_{13}$ nanowires have been reported [12]. One could find the strain-induced formation of 10 nm nanowires of $K_2Ti_6O_{13}$ *via* ion-exchange reaction of $Na_2Ti_3O_7$ in KOH (aq.) [13], synthesis of $K_2Ti_6O_{13}$-*w* by the calcination of KF and TiO_2 powders [14], and synthesis as well as characterization of $K_2Ti_6O_{13}$-*w* with average diameter <100 nm [15]. Comparatively, $K_2Ti_6O_{13}$-*w* has the advantage of lower cost and has been proved to be a suitable substitute for toxic and carcinogenic asbestos used as the matrix material in alkaline fuel cells as it tends to degrade in alkaline solution [16]. It further finds application in photocatalysis [17]. A fibrous crystal of $K_2Ti_4O_{9-x}F_{2x}$ can be obtained from $K_2O–TiO_2–KF$ melt system in a molten KCl bath [1,18] while the polypropylene composites reinforced by Ramier fibre and $K_2Ti_6O_{13}$-*w* have also been developed [19]. $K_2Ti_6O_{13}$-*w* has been tried as filler to modify PP and high mechanical properties reporting the morphology and performance of $K_2Ti_6O_{13}$-*w* reinforced polypropylene composites [20]. The review of animal and *in vitro* data on biological effects of manmade fibres has also been reported [21].

One of the key privileges to these compounds is that their material properties may be tailored by doping aliovalent transition-metal ions. Because of the low concentration of such *functional centres*, standard bulk characterization techniques are not well suited for their analysis and electron paramagnetic resonance (EPR) unified with the dielectric-spectroscopy becomes the *method-of-choice* for its sophisticated sensitivity and selectivity to characterize these dielectrics. Obviously, a rational starting point for a detailed analysis of the role of *functional centres* in the $K_2Ti_6O_{13}$ (PTO) ceramic system is provided by studying first the *pure member*, PTO

---

[*] Corresponding author. Tel.: +91 522 2890812; fax: +91 522 2890809.
E-mail address: svv28srf@gmail.com (S.V. Vikram).

0925-8388/$ – see front matter © 2009 Elsevier B.V. All rights reserved.
doi:10.1016/j.jallcom.2009.09.157

Table 1
List of pure ($x = 0$)[a] and copper doped $K_2Ti_6O_{13}$ ($0.01 \leq x \leq 0.1$) ceramic samples with unit cell volume and lattice parameters.

Cu-doping	Lattice parameters				
	U^b (Å^3)	a (Å)	b (Å)	c (Å)	β (°)
$x = 0.0$[a]	532.76	15.593	3.796	9.108	99.78
$x = 0.01$	523.03	15.4575	3.7921	9.0559	99.83
$x = 0.05$	522.11	15.4358	3.7907	9.0587	99.93
$x = 0.10$	514.07	15.2982	3.7847	9.0100	99.79

[a] S.V. Vikram, D.M. Phase, V.S. Chandel, J. Mater. Sci.:Mater. Electron. (2009) accepted. (Ref. [22]); E. Anderson et al., ibid. and JCPDS file no.:40-0403 ($\lambda = 1.5418$ Å) and ICDS file no.:74-0275 ($\lambda = 1.5406$ Å) (Refs. [26,27]).

[b] Unit cell volume.

[22]. As Cu^{2+} centre is often used as additive during sintering in order to obtain dense ceramics, it is important to enlighten in which way Cu^{2+}-dopants impact the defect chemistry. Acceptor dopants are generally of lower valence than the ion they substitute, resulting in a "hard" compound. On doping with Cu^{2+}, because of its high diffusivity and solubility, predominantly, charge compensation process evolves oxygen vacancies ($V_O^{\bullet\bullet}$), which in turn are, generally, the dominant charge carriers in ceramic oxides and modify the ligand symmetry around the dopant. Acceptor-doped ceramics with high $V_O^{\bullet\bullet}$ concentration show increased change of their electrical properties with time; the phenomenon being termed as *ferroelectric aging* is commonly understood as time restricted domain-wall motion [23]. It is typically accompanied by an increasing shift of the hysteresis loop along the field axis termed as *internal bias field* proposed occurring due to the relaxation of *defect dipoles* formed by the association of $V_O^{\bullet\bullet}$ with the acceptor dopants [24].

Alternatively, PbO-*based* ceramics are widely used for ferroelectric applications due to their excellent *ferroelectric* property [25]. However, volatilization of lethal PbO during high-temperature sintering not only causes environmental pollution but also engender unstability of composition and electrical properties of products. Therefore, it is imperative to develop Pb-*free* ceramics to replace Pb-*based* ceramic. The potential industrial application and interesting behaviour of this alkali titanate is the motivation to study this material thoroughly.

2. Experimental

$K_2Ti_6O_{13}$ (PTO) ceramic was prepared by conventional solid-state route taking stoichiometric amounts of the grinded AR grade K_2CO_3 and TiO_2 powders (Purity ~ 99.9%), under acetone and calcined at 1000 °C for 24 h followed by furnace cooling. The grinded powder after compaction at 15 MPa was sintered at 1000 °C for 1 h. To prepare copper doped ($x = 0.01, 0.05, 0.10$) specimens, desired amount of CuO powder (Purity ~ 99.9%; AR grade) was added to the mixture of alkali carbonate and TiO_2 and the mass so obtained was recycled through the above process. Room temperature (RT) XRD spectrum of all the specimens were obtained on an X-ray powder diffractometer (Rigaku; Model: SC-30; Category No. 5738 E-1) operating at 100 mA and 40 kV using Cu K_α radiation ($\lambda = 1.5418$ Å) with sweep = 3°/min, and $T = 10$ s.

Surface morphology of all the specimen was studied using SEM (Model: JEOL JSM 5600). The usual first derivative of X-band (9.858 GHz) EPR absorption spectra were recorded on a Bruker EMX X-band EPR spectrometer. The high frequency modulation field amplitude ranged typically from 0.005 to 0.5 mT with rectangular TE_{102} cavity (unloaded $Q \sim 7000$) at 100 kHz field modulation. Moreover, samples were kept in ~4 mm quartz tube placed at the centre of resonant cavity. The dielectric-spectroscopic measurements were carried out on an HP 4192A impedance analyzer.

3. Results and discussion

3.1. XRD and structural analysis

Fig. 1 shows the XRD patterns, achieved at RT, for pure and copper doped ($x = 0, 0.01, 0.05, 0.1$) $K_2Ti_6O_{13}$ ceramics which confirm their single phase formation. Lattice constants evaluated from these patterns and provided in Table 1 disclose their monoclinic crystal symmetry isostructural to undoped $K_2Ti_6O_{13}$ ceramic [26,27]. Moreover, one can see from Table 1 that the values of lattice parameters a and b decrease with copper doping ($x = 0$–0.1). However, parameter c first increases for less doping ($x = 0.01$) but it gets decreased for further heavy dopings ($x = 0.05, 0.10$). The angular lattice parameter β also follows a similar pattern. Hence, we can observe that doping invariably and consistently shrinks the unit cell volume. If we consider the schematic structure of $K_2Ti_6O_{13}$, it may be described having K^+ ions in the tunnel space contributing in the ionic conduction while TiO_6 (or CuO_6) assembly is attached with each other forming zigzag ribbons joined by edge-sharing.

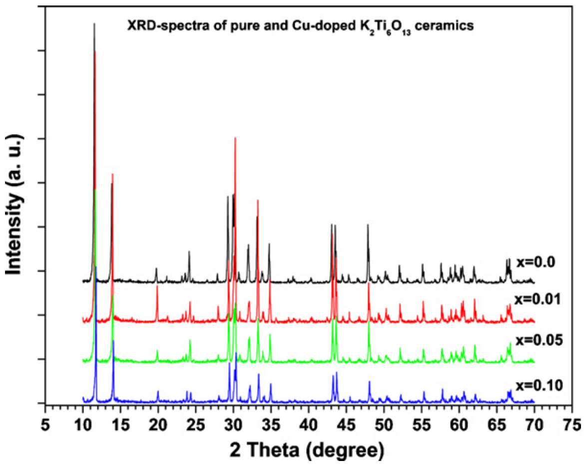

Fig. 1. XRD spectra (Cu K_α) of pure and copper doped ($x = 0, 0.01, 0.05, 0.1$) $K_2Ti_6O_{13}$ ceramics, recorded at RT, showing monoclinic crystal structure.

3.2. SEM and microstructure

Fig. 2(a)–(d) illustrates the SEM pictures for all the pure and copper doped ($x = 0.01, 0.05, 0.1$) specimens of the $K_2Ti_6O_{13}$ ceramic. These micrographs demonstrate that the particle shapes for pure and doped specimens are microtubular with average width of ~1–4 μm and length varying from ~10 to 15 μm. The average grain size decreases as doping level is increased. A rod-like particle with a length of ~10–20 μm grew in the calcination process. Many needle like particles grew on the surface of the rod-shaped particle with average cross-sectional width of ~1–2 μm. As copper doping increases, the whisker like structures start forming agglomerates and the length of rod-like structures disappears. The growth of rod-like particles is due to the crystal structure of TiO_2 and $K_2Ti_6O_{13}$. It is easy to form a tunnel structure of $K_2Ti_6O_{13}$ by the reaction at the solid–liquid interface between solid TiO_2 and liquid K_2O as well as the chain structure of TiO_2 (rutile) composed of several TiO_6 octahedra [28,29].

3.3. EPR spectroscopy

The first derivative of X-band (9.858 GHz) EPR absorption spectra for all the specimens ($x = 0, 0.01, 0.05, 0.1$) were recorded at RT and the resulting data is shown in Fig. 3(a). The g-value is defined as $g = h\nu/(\beta B_0)$ where h is the Planck's constant, β the Bohr magneton, ν the resonance frequency of the sample cavity and B_0 is the centre of the resonance absorption signal.

The signals at 892 G ($g \sim 7.91$), 1298 G ($g \sim 5.43$), and 1541 G ($g \sim 4.58$) show the presence of axial components of $(Fe'_{Ti}-V_O^{\bullet\bullet})$ *defect associate dipoles* in the orthorhombic symmetry due to Fe^{3+} present as an intrinsic impurity in the starting materials [30,31]. During high-temperature sintering, this iron forms defect associate dipoles due to iron–oxygen vacancy defect association. This con-

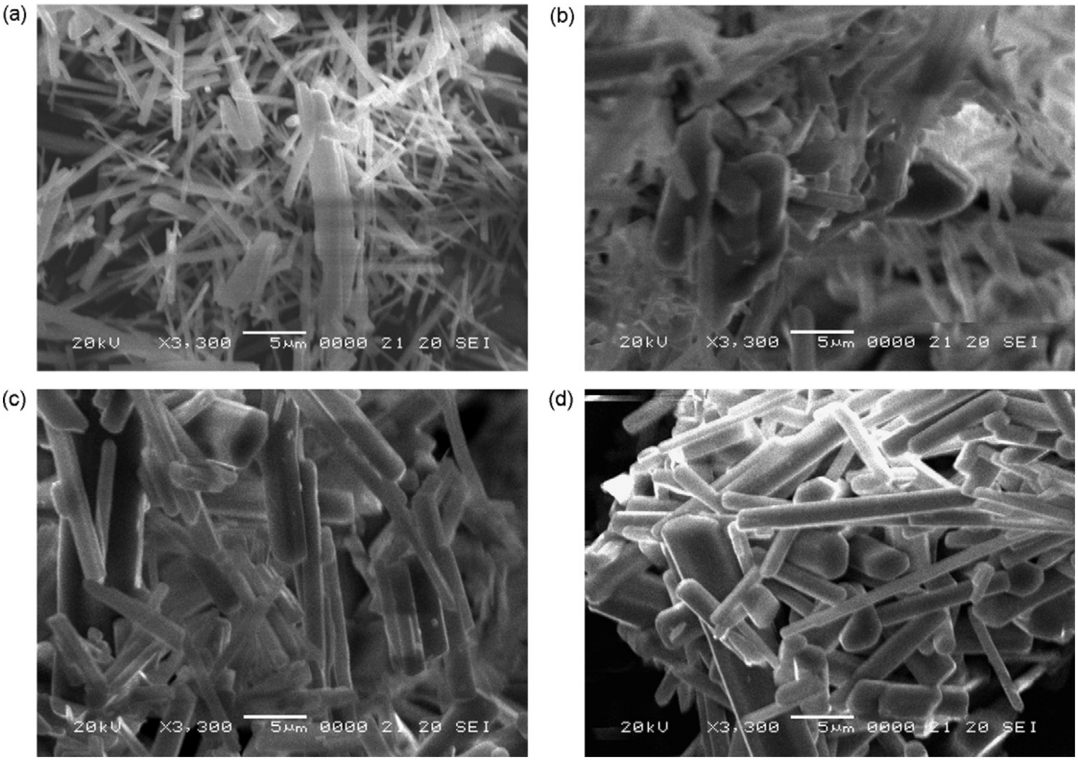

Fig. 2. SEM pictures of $K_2Ti_6O_{13}$ and its Cu-doped ($x = 0$, 0.01, 0.05, 0.1) derivatives after densification showing particle shape to be microtube like.

cept may be upheld due to the presence of all these signals in the undoped ($x = 0$) specimen. The spin-Hamiltonian for this centre may be written as:

$$\mathbf{H_S} = g_{\|}\beta H_z S_z + g_{\perp}\beta(H_x S_x + H_y S_y) + D\left[\frac{S_z^2 - 1}{3S(S-1)}\right], \qquad (1)$$

where $g_{\|}$ ($g_{\perp}$) is the g-value parallel (perpendicular) to the symmetry axis, S is the electron spin and D is the zero field splitting parameter. The signal at $g \sim 5.43$ is characteristic of an $S = 5/2$ system, which is orbitally nondegenerate in an octahedral field with a very strong nearly tetragonal distortion [30–33].

The fact that $g \sim 5.43$ strongly suggests that at X-band frequencies, the frequency of observation is much less than the splitting of the energy levels of Eq. (1) at zero magnetic field strength, i.e., $D \gg h\nu$. This spectrum has been identified as a $(\mathrm{Fe}'_{\mathrm{Ti}}\text{–}\mathrm{V_O}^{\bullet\bullet})$ centre, which is a defect–dipole complex [30,31,34]. The Fe^{3+} ion has substituted for the Ti^{4+} ion and is negatively charged and $\mathrm{V_O}^{\bullet\bullet}$ is doubly positively charged with respect to the neutral lattice. It is believed that the nearby $\mathrm{V_O}^{\bullet\bullet}$ causes the large tetragonal distortion of the $(\mathrm{Fe}'_{\mathrm{Ti}}\text{–}\mathrm{V_O}^{\bullet\bullet})$ centre [30].

The other centre at 1846 G ($g \sim 3.82$) is also characteristic of a defect that is in an octahedral field with a very strong tetragonal distortion, except that $S = 3/2$ [33–35]. Following our earlier arguments, the fact that $g_{\perp} \sim 3.82$ strongly suggests that $D \gg h\nu$. To calculate D, $g_{\perp}$ and $g_{\|}$ for this signal, it is necessary to carry out EPR at two differing microwave frequencies, which could not be done in this study. The atomic nature of this $g \sim 3.82$ signal is not precisely known, however, it has been attributed to defect–dipole complexes such as $(\mathrm{Fe}'''_{\mathrm{Ti}}\text{–}\mathrm{V_O}^{\bullet\bullet})$ centre [33]. It is assumed that the large tetragonal field also arises from a nearby vacancy. Moreover, the smearing of these signals may be due to the excessive isotropic exchange interaction. The signal with $g \sim 1.87$ must be attributed to Ti^{3+} ($3d^1$) species present in the specimens and the low intensity level of this signal shows that very little amount of Ti^{3+} were present in the specimens [36]. The influencing oscillating a.c. field would easily reorient the deficiency related $(\mathrm{Fe}'_{\mathrm{Ti}}\text{–}\mathrm{V_O}^{\bullet\bullet})$ dipoles through electron hopping [37].

The spectrum for isolated Cu^{2+} signals (near $g \sim 2.0$) may be bifurcated corresponding to two distinct locally distorted environments of Cu^{2+} substituting Ti^{4+} sites. While the spectrum for four hyperfine signals with $g_{\|} \sim 2.42$ (2700–3010 G) and its similar asymmetric counter-spectra with $g_{\perp} \sim 2.04$ (3450–3700 G) correspond to copper at Ti^{4+} site having distorted local surrounding of first kind (*viz.* $\mathrm{Cu}^{2+}_{\mathrm{Ti}}$ (2)), signals with $g_{\|} \sim 2.23$ (3000–3315 G) and its counter-spectra with $g_{\perp} \sim 2.08$ (3350–3460 G) correspond to distorted local environment of second kind (*viz.* $\mathrm{Cu}^{2+}_{\mathrm{Ti}}$ (1)) [36,38,39]. The spectrum for four hyperfine (HF) signals of both the isolated centres, $\mathrm{Cu}^{2+}_{\mathrm{Ti}}$ (1) and $\mathrm{Cu}^{2+}_{\mathrm{Ti}}$ (2), discussed above may be explained by an isotropic spin-Hamiltonian:

$$H = g\beta(\vec{\mathbf{B}}\cdot\hat{\mathbf{S}}) + \frac{1}{2}A(\hat{\mathbf{S}}\cdot\vec{\boldsymbol{I}}) + \sum_{i+1}^{N} a_i(\hat{\mathbf{S}}\cdot\vec{\boldsymbol{I}}_i) \qquad (2)$$

and g-components are

$$g_{\|} = g_z \quad \text{and} \quad g_{\perp} = \frac{g_x + g_y}{2} \qquad (3)$$

where the first term is Zeeman interaction, and the second and third terms are HF and SHF interactions. $\boldsymbol{I}_i$ is the nuclear spin of Ti-ions. Since the stable isotopes ^{63}Cu (69.2%) and ^{65}Cu (30.8%) have same nuclear spin ($\boldsymbol{I} = 3/2$) with only a small difference between their nuclear magnetic moments, the isotope splitting is undetectable in this EPR-spectra and thus could be neglected. For fine structure (FS) spectrum, the $g_{\|}$ and $g_{\perp}$ components of the g-tensor correspond to the four lines above the baseline and below the baseline, respectively [36]. The broadening of HF signal line width for second copper centre, on increased doping as apparent in Fig. 3(b), suggests that $\mathrm{Cu}^{2+}_{\mathrm{Ti}}$ (2) undergoes dipole–dipole interaction and that crystal symmetry around this ion is affected by the dopant concentration in the host lattice.

Table 2
Spin-Hamiltonian parameters, for Cu-doped $K_2Ti_6O_{13}$ ($0.01 \le x \le 0.1$) ceramics, obtained by X-band EPR-spectra recorded at RT.

Sample doping	Cu^{2+}_{Ti} (1)				Cu^{2+}_{Ti} (2)				(Fe'_{Ti}–$V_O^{\bullet\bullet}$)		
	$g_\parallel$ (±0.0001)	$g_\perp$ (±0.0001)	$A_\parallel$ (±1)	$A_\perp$ (±1)	$g_\parallel$ (±0.0001)	$g_\perp$ (±0.0001)	$A_\parallel$ (±1)	$A_\perp$ (±1)	g_z (±0.0001)	g_y (±0.0001)	g_x (±0.0001)
$x = 0.0$	–	–	–	–	–	–	–	–	7.9127	5.4346	4.5789
$x = 0.01$	2.2300	2.0811	101	23	2.4314	2.0413	73	67	7.9127	5.4346	4.5789
$x = 0.05$	2.2300	2.0811	101	23	2.4151	2.0425	71	68	7.9127	5.4346	4.5789
$x = 0.10$	2.2300	2.0811	101	23	2.4216	2.0425	68	70	7.9127	5.4346	4.5789

Since the balance between ligand field asymmetry and the natural tendency of Cu^{2+}_{Ti} to adopt tetragonally elongated octahedral coordination geometry results in a complex with orthorhombic coordination geometry which eventually attains axial symmetry [40], the same could also be upheld for the above investigation. The observed relationship among the principal *g*-values $g_\parallel > g_\perp > g_{\text{free electron}}$ (=2.0023) of the two EPR-spectra are expected for ions with the $3d^9$ configuration at distorted octahedral sites [41,42]. Analysis of the calculated FS *g*-values and HFS *A*-values listed in Table 2 indicate that probably the splitting occurs in the octahedral symmetry and copper site attains Cu^{2+}_{Ti} at Ti^{4+}_{Ti} host-site with two distinct distorted local environments. Under the influence of an octahedral crystal field, the fivefold-degenerate 3d orbital is splitted into a t_{2g} (triplet) and a e_g (doublet). In this case, Jahn–Teller effective distortion splits the deeper lying electron state e_g of the $3d^9$ configuration. Thus, in general, four transitions are possible among such levels. The *g*-values also suggest that the Cu^{2+} ions are in the $|x^2 - y^2\rangle$ state which leads to elongation of the octahedral environment along the tetragonal axis and this deformation may be created by one or two $V_O^{\bullet\bullet}$ in the Cu^{2+} environment. The introduction of $V_O^{\bullet\bullet}$ by Cu-doping also leads to a slight reduction in unit cell size [43] and hence resulting in the contraction of tunnel space available for ionic conduction. This doping may further contract the tunnel space between adjacent Ti–Ti chains due to bigger ionic size of Cu^{2+} than Ti^{4+}.

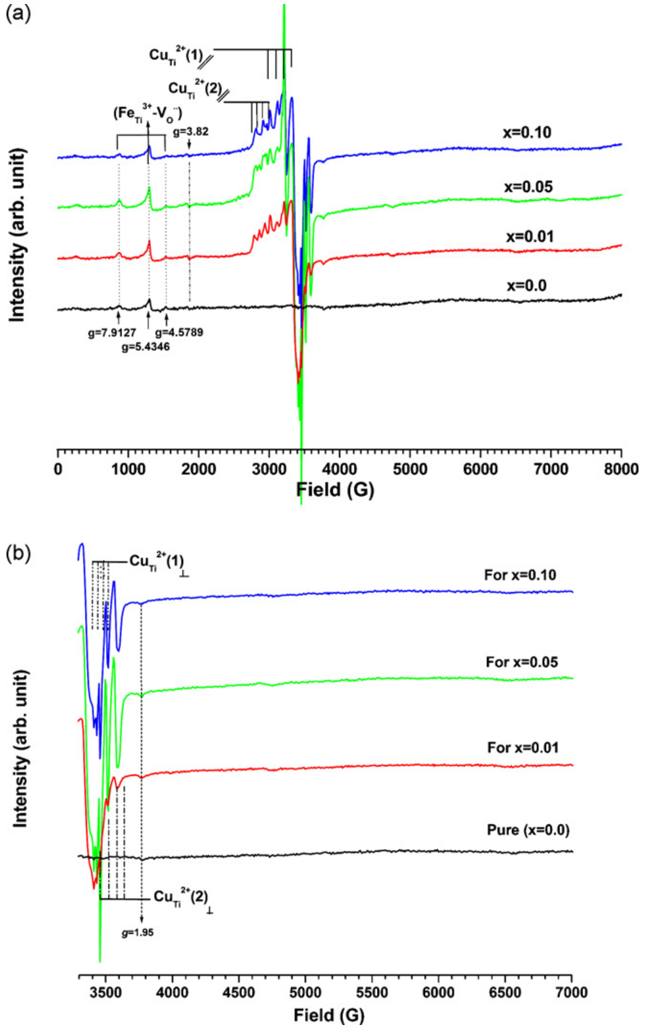

Fig. 3. First derivative of X-band (9.858 GHz) EPR-spectra achieved at RT for $K_2Ti_6O_{13}$ and its Cu-doped ($x = 0, 0.01, 0.05, 0.10$) derivatives showing FS and HFS spectra. Low-field signals show the presence of (Fe'_{Ti}–$V_O^{\bullet\bullet}$) *defect associate dipoles* in pure and doped specimens.

3.4. Electrical characterization

3.4.1. Thermal response

The loss tangent ($\tan\delta$) and parallel capacitance (C_p) of the ceramic pellets were measured directly from the impedance analyzer. However, relative permittivity (ε_r) was calculated using relation

$$\varepsilon_r = \frac{C_p}{\varepsilon_o(a/t)} \tag{4}$$

where *t* is thickness and *a* being cross-sectional area of the pellet. Fig. 4(a)–(d) elucidates the thermal behaviour of dielectric permittivity and dielectric loss corresponding to 100, 400, and 800 kHz frequencies for all the pure and doped specimens ($x = 0, 0.01, 0.05, 0.1$). As compared to pure specimen, the loss pattern in all the doped compositions ($x = 0.01$–0.1) attains stabilization to a larger extent, resulting in two broad relaxation peaks in $x = 0.05$ and one in $x = 0.1$ doped compositions. This may be accredited to the homogeneity in the composition on dopant incorporation in the lattice but oxygen vacancies that stabilize the structure also lead to high mobility in the oxygen sub-lattice (CuO_6 and TiO_6) and to behave as a fast-ion conductor [43]. For pure sample ($x = 0$), one could mark almost zero frequency dispersion for relative permittivity up to $T \sim 220\,°C$. The loss patterns also follow the similar trend. A *ferroelectric–paraelectric* type transition may be identified at $T_{C1} \sim 300\,°C$ showing strong frequency dispersion [22] and a transition accompanying the sudden fall in permittivity and loss values near $T \sim 420\,°C$ is also evident. On less copper doping ($x = 0.01$), the non-dispersive zone shifts to higher temperatures (~250 °C). Moreover, the peak at $T_C \sim 300\,°C$ broadens and gets shifted to ~470 °C while $\tan\delta$ gets enhanced in the same composition without affecting permittivity to a large extent. For growing temperatures, the usual increase in $\tan\delta$ may be due to leakage current and the growth in the number of ions taking part in polarization [44]. However, at higher temperatures, the higher rate of increase of $\tan\delta$ for lower frequencies is due to *space charge polarization* [45].

As the doping is increased to $x = 0.05$, the non-dispersive low-temperate zone (170–240 °C) becomes disturbed and a plateau like structure emerges. The *ferroelectric–paraelectric* type peak occurs at $T_{C1} \sim 370\,°C$ having its corresponding loss peak in its vicinity. Moreover, a second but comparatively sharp *ferroelectric–paraelectric* type phase transition also occurs at $T_{C2} \sim 480\,°C$ showing the higher peak value of dielectric permittivity than the first transition. This can be explained by assuming that in materials exhibiting diffuse

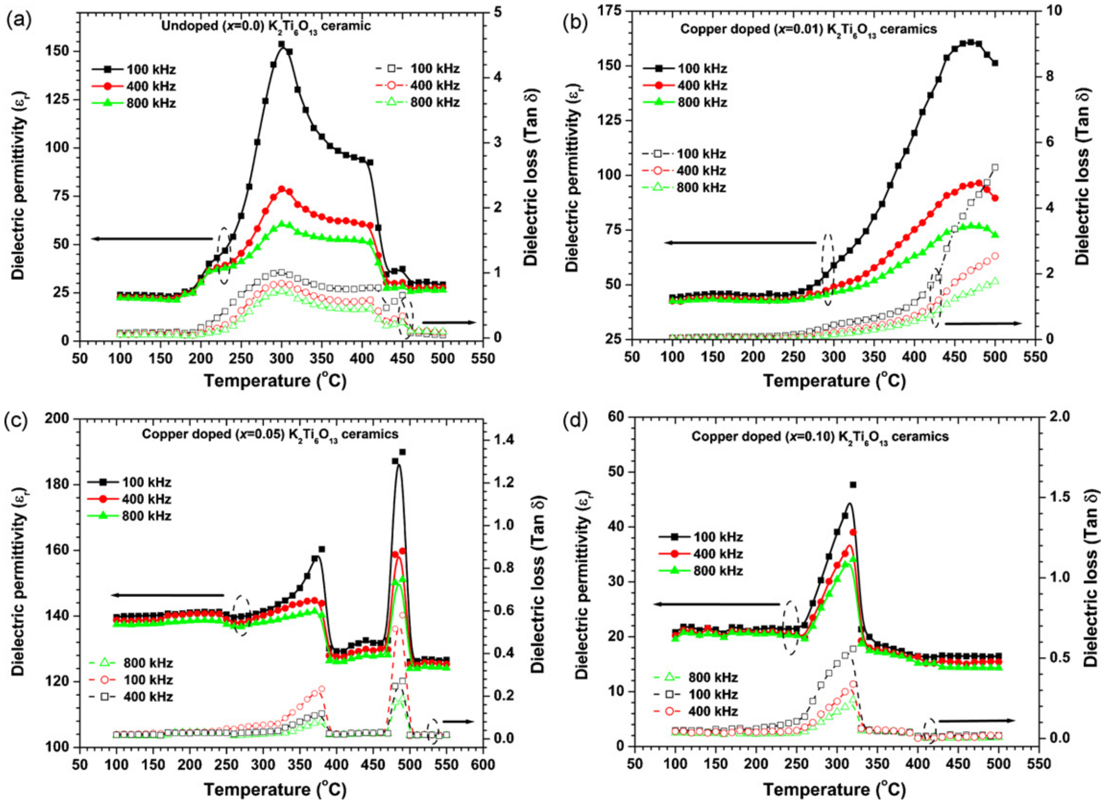

Fig. 4. Dielectric permittivity and loss tangent in function of temperature for $K_2Ti_6O_{13}$ and its copper doped ($x = 0$, 0.01, 0.05, 0.1) derivatives at 100, 400, and 800 kHz frequencies.

phase transitions probably the randomness of the impurity and defect distribution are not homogeneous and if it becomes homogeneous, a sharp transition occurs [46]. Hence, in this specimen, the stabilization of spontaneous polarization is achieved by doping of copper in the lattice.

Now, for heavy copper doping ($x = 0.1$), low-temperate non-dispersive zone remains disturbed but with less degree of disturbance as compared to previous compositions. A *ferroelectric–paraelectric* type peak at $T_C \sim 320\,^\circ\mathrm{C}$ with corresponding tan δ peak near the same temperature can be visualised without any second phase transition. Besides, at $T \sim 400\,^\circ\mathrm{C}$, there is a little downfall in permittivity and loss values. The origin of loss peaks may be recognized to the relaxation of *permanent dipoles* [45] and the ($\mathrm{Fe}'_{\mathrm{Ti}}$–$\mathrm{V_O}^{\bullet\bullet}$) *defect associate dipoles*. As compared to moderate doping ($x = 0.05$), the peak shifts toward the low-temperate region possibly due to change in relaxation time and disorderness introduced in the lattice owing to dopant inclusion. We can also see that the peak first broadens and then sharpens for augmented copper doping indicating that the influence of doping becomes prone at high temperatures and triggers perturbation in the structural symmetry. The broadening of the dielectric peaks observed may be attributed to the disorder introduced in the lattice due to $\mathrm{Cu}^{2+}_{\mathrm{Ti}}$ leading to heterogeneity in the microcomposition as reflected well in the EPR studies. On the other hand, oxygen vacancies ($\mathrm{V_O}^{\bullet\bullet}$) formed due to $\mathrm{Cu}^{2+}_{\mathrm{Ti}}$ ions cause deformation of the surrounding volume and modification of the local fields.

The origin of phase transitions in the pure and doped compositions showing dielectric anomaly may be explained by assuming that after the failure of lattice to relax against lattice stresses, TiO_6 octahedral assemblies are heavily distorted and the central Ti^{4+} ion gets off-centre in an intact oxygen octahedron following the emergence of *permanent dipoles*. These dipoles tend to reorient themselves in the direction of applied field, thereby producing strong polarization effects and hence showing presence of spontaneous polarization in all the compositions. As temperature advances above T_{C1} or T_{C2}, intensified thermal vibrations demolish the ordering of spontaneous polarization resulting in the drop off in the relative permittivity (ε_r) values and therefore relative permittivity peaks at T_{C1} or T_{C2} indicating normal *ferroelectric–paraelectric* type phase transition due to spontaneous polarization. This fact is maintained by the evidence of huge dissipation of energy and temperature dependency of loss tangent at the same temperatures. Here, strong Jahn–Teller effect (JTE) due to the $3d^9$ configuration of $\mathrm{Cu}^{2+}_{\mathrm{Ti}}$ in the octahedral oxygen environment seems to represent the driving force for this phase transition [36]. Noticeably, these phase transitions take place provided the concentrations of both, oxygen vacancies and the JTE active accepter ions, along with ionic mobilities are high enough [42]. At this point, the local lattice distortions may kick off the phase transitions and lower the transition temperatures of the doped compositions. Accordingly, these materials may constitute a new family of Pb-free ceramic ferroelectrics.

The augmentation of oxygen vacancies ($\mathrm{V_O}^{\bullet\bullet}$) also introduces space charges and by this means an internal bias field sets inside the grains inhibiting the domain motion. Thus, domain walls get pinned by these vacancies [47]. Compared to the ionic mobility of free $\mathrm{V_O}^{\bullet\bullet}$, ($\mathrm{Fe}'_{\mathrm{Ti}}$–$\mathrm{V_O}^{\bullet\bullet}$) complex will be rather immobile in the ceramic specimen considerably hindering charge transport. This defect dipole may also influence the poling properties by providing pinning centres for domain walls [48].

The broad nature of peaks indicate a diffuse *ferroelectric* phase transition showing relaxor ferroelectric behaviour since, in transition materials, each micro-volume transfers at a different temperature, spreading out these heat changes and subsequently reducing the sharp peak to a general rounded hump [49]. However, the broadening also occurs due to the inhomogeneous nature of the internal field due to ($\mathrm{Fe}'_{\mathrm{Ti}}$–$\mathrm{V_O}^{\bullet\bullet}$) *defect associate dipoles* [46]. As $\mathrm{V_O}^{\bullet\bullet}$ are associated with $\mathrm{Fe}'_{\mathrm{Ti}}$ centres, any clustering of $\mathrm{V_O}^{\bullet\bullet}$ seems to be rather unlikely. However, such defect clusters have been proposed

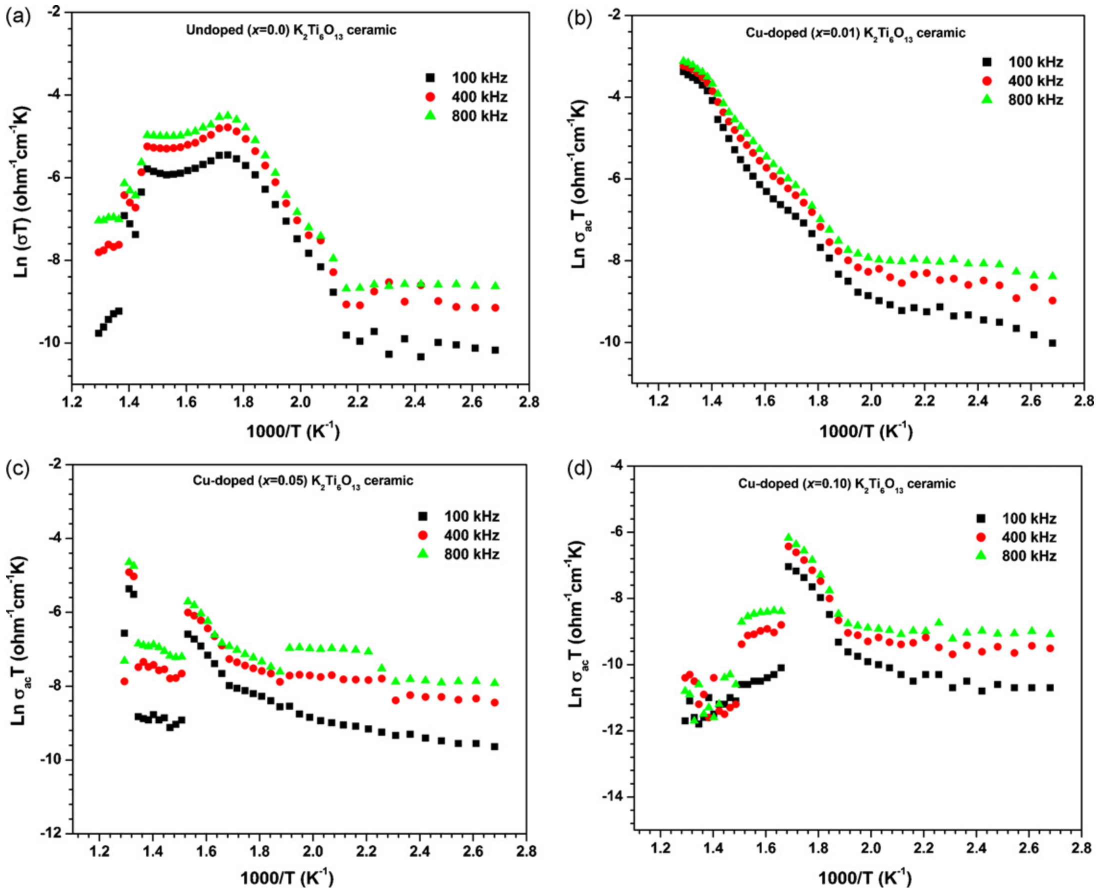

Fig. 5. a.c. conductivity in function of temperature for $K_2Ti_6O_{13}$ and its copper doped ($x = 0$, 0.01, 0.05, 0.1) derivatives.

to exist related to localized polaron states, as which the majority of electron states in perovskite oxides have been identified, promoting only a small fraction of electrons into the conduction band [50]. Owing to the observed $(\mathrm{Fe}'_{\mathrm{Ti}}\text{–}\mathrm{V_O}^{\bullet\bullet})$ association and subsequently reduced mobility of $\mathrm{V_O}^{\bullet\bullet}$, this hypothesis thus cannot be upheld for Cu-modified $K_2Ti_6O_{13}$ ceramics.

The bulk a.c. conductivity ($\sigma_{\text{a.c.}}$) values of the sample at different frequencies have been calculated using the relation:

$$\sigma_{\text{a.c.}}(\omega) = 2\pi f\left(\frac{t}{a}\right) C_{\text{p}} \tan\delta \tag{5}$$

Fig. 5(a)–(d) illustrates the a.c. conductivity in function of temperature for 100, 400, and 800 kHz frequencies in the temperature range of 100–500 °C. Except less doped ($x = 0.01$) sample, all other samples show slightly nontypical patterns for thermal behaviour of a.c. conductivity. The trend may be analysed by grouping it into four regions:

- **Region-I** (100–250 °C). A low-temperate region with low activation energy could be recognized in all the doped specimens but this region shrinks with Cu-doping. In this region, strong frequency and temperature dependency of a.c. conductivity is observed for all the compositions. Such trends, related to ω^s (where $s < 1$) are the outcome of electron-hopping (polaron) conduction [5]. The trend of variation of conductivity in this region is similar in all the doped specimens except for a decrease in the frequency dependence and increase in the temperature dependence. In addition, low activation energy values in this region boost the possibility of polaron conduction.
- **Region-II** (250–350 °C). In this region, $\sigma_{\text{a.c.}}$ is frequency as well as temperature dependent and also shows higher slope than region-I for all the doped specimens. It indicates the presence of exchangeable intratunnel ionic conduction and temperature dependency is due to multiple hops [51]. Moreover, frequency dependency becomes linear with elevated slope as the amount of copper increases in the lattice, suggesting that bigger copper ions are accommodated along with smaller Ti-ions in the lattice. Furthermore, since frequency dependency persists in this region, electron-hopping conduction also exists [5].
- **Region-III** (350–400 °C). The conductivity in this region is of anomalous nature giving rise to peaking and then slight downfall in all the pure and doped compositions except $x = 0.01$ doped composition which shows a smooth linear trend. Strong dipolar mechanism dominates with the increase in doping and it is responsible for the peaks in all the doped specimens. It can also be seen that the position of peaks changes in all the specimens due to change in relaxation time and disorderness introduced in the lattice. Thus, unassociated intratunnel ionic conduction along with suppressed electron-hopping conduction exists in this region [5].
- **Region-IV** (400–500 °C). In this region, results show that a.c. conductivity increases with temperature, but the activation energies for all the specimens have same values despite increase in the doping. Moreover, least but linear frequency dependency is seen. The temperature dependency in $x = 0.10$ becomes negligible as it attains almost constant values of conductivity showing the persistence of associated intratunnel ionic conduction.

Besides, as the temperature grows, the activation energy increases saturating at the highest temperature recorded. The average value of a.c. conductivity increases for less and moderate dopings ($x = 0.01$, 0.05) but, further, it depreciates for heavy doping ($x = 0.1$).

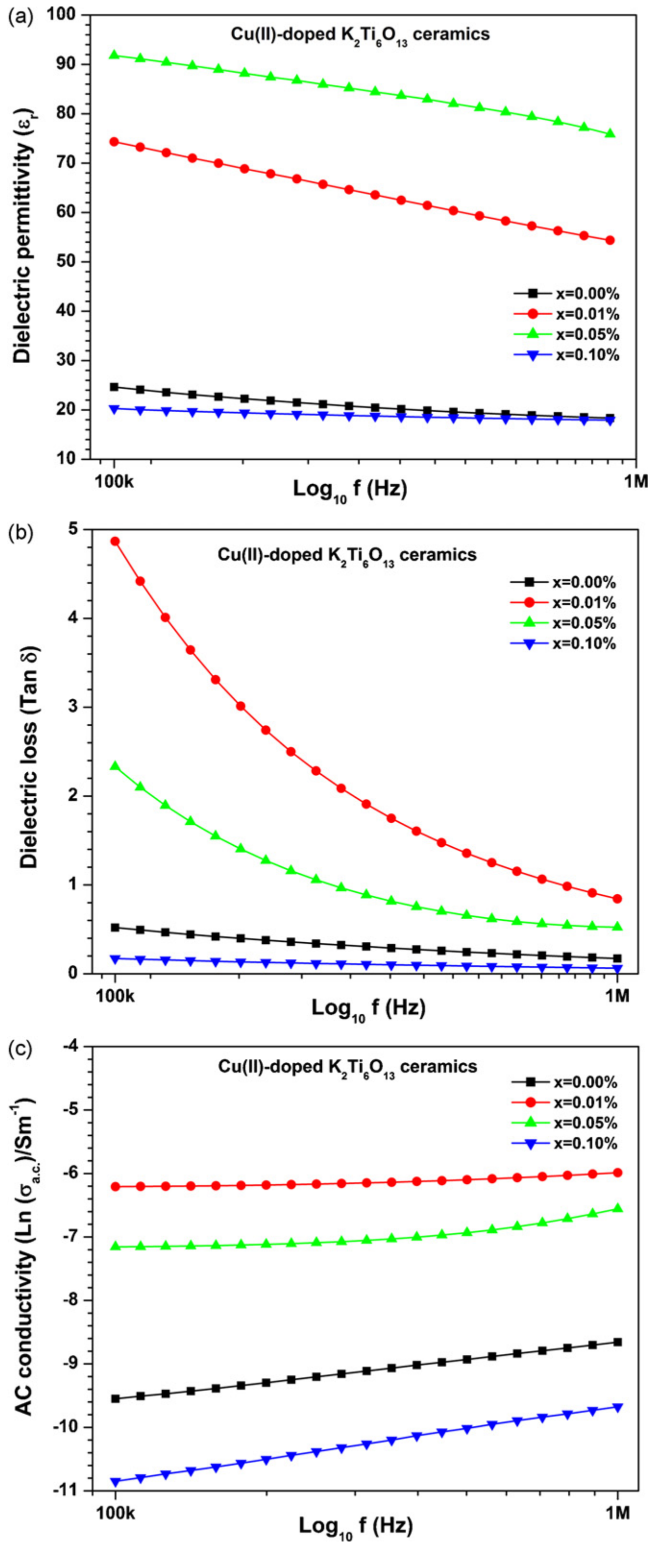

Fig. 6. (a) Dielectric permittivity, (b) loss tangent, and (c) a.c. conductivity in function of frequency for $K_2Ti_6O_{13}$ and its copper doped ($x = 0, 0.01, 0.05, 0.1$) derivatives recorded at RT.

3.4.2. *Frequency response*

Fig. 6(a) shows the frequency response of dielectric loss, achieved at RT, in the frequency range of 100–1000 kHz for $x = 0$, 0.01, 0.05, and 0.1, respectively. We can mark the exponential demise of losses for all the ceramic specimens. Less doping ($x = 0.01$) increases dielectric losses to very high values as compared to pure one ($x = 0$). However, further doping causes the decrease in losses to a significant limit. For heavy doping ($x = 0.1$) any further, dielectric losses are decreased to very low values even below the values for undoped sample ($x = 0$). However, losses decrease exponentially with the application of a.c. field owing to the fact that at higher frequencies, ceramic specimens offer low reactance to the sinusoidal signal and hence minimize the conduction losses [44]. Therefore, dielectric losses decrease at higher frequency. These types of variations in the dielectric losses are characteristic of the dipole orientation and electrical conduction [52,53].

Fig. 6(b) shows the frequency response of dielectric permittivity data, recorded at RT, in the frequency range of 100–1000 kHz for $x = 0$, 0.01, 0.05, and 0.1, respectively. One could observe the increasing trend of ε_r values with doping variation of $x = 0$–0.05. However, for heavy doping ($x = 0.1$), it falls down even below values for undoped sample ($x = 0$). Besides, ε_r values diminish with increasing frequency.

Fig. 6(c) shows the room temperature frequency response of a.c. conductivity ($\ln(\sigma_{a.c.})$) in the range of 100–1000 kHz for $x = 0$, 0.01, 0.05, and 0.1, respectively. It shows a consistent increase with frequency for all the samples except the fact that this trend is more pronounced for heavy doping. Similar to loss patterns, less doping ($x = 0$–0.05) augments a.c. conductivity values while heavy doping ($x = 0.1$) reduces them significantly. This is because they get increased for $x = 0.01$ due to increased spin–phonon interaction as evident from the broadening of EPR signal and also due to the dominance of electron-hopping conduction. The values decrease for $x = 0.05$ and $x = 0.1$ doping due to shrinkage of the tunnel space on dopant entry in the lattice resulting in the hindrances suppressing ionic conduction and also due to the trapping of conduction electrons by Cu^{2+} from nearby oxygen ions. The concentration of Cu^{2+} ions in the base matrix of $K_2Ti_6O_{13}$ sets up such a configuration which suppresses electron-hopping conduction. Hence, it seems that the structural configuration responsible for hopping conduction suppresses intratunnel ionic conduction.

4. Conclusions

$K_2Ti_6O_{13}$ and its copper doped ($x = 0.01, 0.05, 0.1$) ceramic specimens were synthesised using solid-state route. Lattice constants evaluated from room temperature XRD spectra revealed the phase formation in a monoclinic symmetry. Surface morphology was studied using SEM pictures exposing microtubular particles. X-band EPR-spectra, achieved at RT, were found to show that Cu^{2+} occupied Ti^{4+} sites with two distinct locally distorted surroundings identified by the high-field four HFS signals each smearing with augmented copper doping due to excessive dipole-dipole interactions. The low-field spectrum ($g \sim 5.43$) identified (Fe'_{Ti}–$V_O^{\bullet\bullet}$) *defect associate dipoles* produced due to iron–oxygen vacancy association exhibiting slight broadening on dopant augmentation due to increased isotropic exchange interaction.

Doping was primarily found to increase the dielectric losses due to space charges but further it caused decrease due to inhibition of domain-wall motion. The loss mechanism together represented electrical conduction, dipole orientation, and space charges. Besides, *ferroelectric–paraelectric* type phase transitions were identified at $T_C \sim 300$ ($x = 0$), 370 ($x = 0.01$), 370 and 480 ($x = 0.05$), and 320 °C ($x = 0.1$), respectively.

While slight doping augmented a.c. conductivity values due to increased spin–phonon interaction as well as due to the domination of polaron conduction, heavy doping reduced it due to shrinkage of the tunnel space and the trapping of conduction electrons by Cu^{2+} from nearby oxygen ions. Hence, the structural configuration responsible for hopping conduction simultaneously curbed the intratunnel ionic conduction.

Acknowledgements

Authors gratefully recognize the experimental support extended by DAE–UGC Consortium for Scientific Research, Indore, India against SEM and XRD facilities and also thank Mr. S. Bharadwaj and Mr. V. Ahire of this centre for such assistance.

References

[1] K.L. Berry, et al., J. Inorg. Nucl. Chem. 14 (1960) 231.
[2] M.L. Granvalet-Mancini, et al., Eur. J. Solid State Inorg. Chem. 31 (1994) 767.
[3] (a) S.V. Vikram, D. Maurya, V.S. Chandel, Mater. Sci. (Poland) 27 (1) (2009) 193;
(b) S.V. Vikram, D. Maurya, V.S. Chandel, J. Alloys Compd. 478 (2009) 398;
(c) S.V. Vikram, V.S. Chandel, Int. J. Mech. Eng. Mater. Sci., in press.
[4] S.V. Vikram, D. Maurya, V.S. Chandel, (2009) comm.
[5] (a) D. Maurya, J. Kumar, Shripal, J. Phys. Chem. Solids 66 (2005) 1614;
(b) D. Maurya, J. Kumar, Shripal, J. Appl. Phys. 100 (2006) 034103-1;
(c) D. Maurya, Premchand, J. Alloys Compd. 459 (2008) 418.
[6] S. Kikkawa, M. Koizumi, in: S. Saito (Ed.), Fine Ceramics, Else. Publ. Co., USA, 1988, pp. 83–90.
[7] G.L. Li, G.H. Wang, J.M. Hong, J. Mater. Sci. Lett. 18 (1999) 1865.
[8] G.H. Du, et al., Phys. Rev. B 67 (2003) 035323.
[9] G. Guan, et al., Appl. Catal. A 249 (1) (2003) 11.
[10] K. Sayama, H. Arakawa, J. Photochem. Photobiol. A 77 (1994) 243.
[11] B.L. Wang, et al., Chem. Phys. Lett. 376 (2003) 726.
[12] L.M. Torres-Martinez, et al., J. Mater. Online 1 (2005) 1.
[13] B.L. Wang, et al., Appl. Phys. Lett. 86 (3) (2005) 133101.
[14] G.L. Li, G.H. Wang, J.M. Hong, Mater. Res. Bull. 34 (4) (1999) 2341.
[15] Y. Fujiki, JSAE Rev. 6 (1998) 91.
[16] H.-K. Lee, et al., Mater. Chem. Phys. 45 (1996) 243.
[17] S. Ogura, M. Kohno, K. Sato, Y. Inoue, Appl. Surf. Sci. 121/122 (1997) 521.
[18] K.L. Berry, U.S. Patent, 2,841,470 (1958).
[19] C.-G. Long, L.P. He, Z.H. Zhong, S.G. Chen, Res. Lett. Mater. Sci. 2007 (Article Id.: 87072).
[20] S.C. Tjong, Y.Z. Meng, J. Appl. Polym. Sci. 70 (3) (1998) 431.
[21] S.A. Ellouk, M.-C. Jaurand, Environ. Health Perspect. 102 (2) (1994) 47.
[22] S.V. Vikram, D.M. Phase, V.S. Chandel, J. Mater. Sci.:Mater. Electron. (2009) accepted.
[23] P.V. Lambeck, G.H. Jonker, J. Phys. Chem. Solids 47 (1986) 453.
[24] (a) H. Neumann, G. Arlt, Ferroelectrics 76 (1987) 303;
(b) K. Carl, K.H. Härdtl, Ferroelectrics 17 (1978) 473;
(c) G. Arlt, Ferroelectrics 76 (1987) 451.
[25] B. Jaffe, W.R. Cook, H. Jaffe, Piezoelectric Ceramics, Academic, NY, 1971.
[26] (a) S. Anderson, A.D. Wadsley, Acta Crystallogr. 14 (1961) 1245;
(b) O. Plumley, J. Am. Chem. Soc. 83 (1961) 1289;
(c) ICDS Card No.:74-0275.
[27] (a) E. Anderson, I. Anderson, E. Skou, Solid State Ionics 27 (1988) 181;
(b) ICDS Card No.:40-0403.
[28] S. Anderson, A.D. Wadsley, Acta Crystallogr. 15 (1962) 164.
[29] (a) T. Sasaki, Y. Fujiki, J. Solid State Chem. 83 (1989) 45;
(b) Y. Fujiki, T. Mitsuhashi, Ceram. Jpn. 19 (1984) 200.
[30] E. Siegel, K.A. Müller, Phys. Rev. B 19 (1979) 109.
[31] K.A. Müller, J. Phys. 42 (1981) 551.
[32] E.S. Kirkpatrick, K.A. Müller, R.S. Rubins, Phys. Rev. 135 (1964) A86.
[33] J.R. Pilbrow, J. Mater. Res. 31 (1978) 479.
[34] E. Possenriede, et al., Ferroelectrics 92 (1989) 245.
[35] R.L. Berney, D.L. Cowan, Phys. Rev. B 23 (1981) 37.
[36] A. Abragram, B. Bleaney, Electron Paramagnetic Resonance of Transition Ions, Clarendon, Oxford, 1970.
[37] R.K. Dwivedi, D. Kumar, O. Prakash, J. Phys. D 33 (2000) 88.
[38] (a) Langhammer, et al., Solid State Sci. 5 (2003) 965;
(b) Langhammer, et al., J. Eur. Ceram. Soc. 24 (2004) 1489.
[39] A.G. Badalyan, et al., J. Phys.: Condens. Matter 14 (2002) 6855.
[40] H. Headlam, et al., Inorg. Chem. 34 (1995) 5516.
[41] (a) B.J. Hathaway, D.E. Billing, Coord. Chem. Rev. 5 (1970) 143;
(b) D.J. Keeble, Z. Li, M. Marmatz, J. Phys. Chem. Solids 57 (1996) 1513.
[42] (a) W. Warren, B.A. Tuttle, J. Am. Ceram. Soc. 80 (1997) 860;
(b) D.V. Azamat, et al., Ferroelectrics 254 (2001) 77.
[43] A.J. Moulson, J.M. Herbert, Electroceramics, Chapman and Hall Inc., 1990 (Chaps. 4–7).
[44] N.P. Bogoroditsky, V.V. Pasynkov, B. Tareev, Electrical Engineering Materials, Mir Publ., Moscow, 1979 (Chaps. 1 and 3).
[45] B.P. Das, R.N.P. Chaudhary, P.K. Mahapatra, Mater. Sci. Eng. B 104 (2003) 96.
[46] M.E. Lines, A.M. Glass, Principles and Applications of Ferroelectrics and Related Materials, Clarendon, Oxford, 1977, pp. 87, 286.
[47] S.B. Majumdar, B. Roy, R.S. Katiyar, S.B. Krupanidhi, J. Appl. Phys. 90 (2001) 2975.
[48] (a) T.J. Yang, et al., Phys. Rev. Lett. 82 (1999) 4106;
(b) D. Damjanovic, Rep. Prog. Phys. 61 (1998) 1267.
[49] N. Setter, L.E. Cross, J. Mater. Sci. 15 (1980) 2478.
[50] B. Güttler, U. Bismayer, P. Groves, E. Salje, Semicond. Sci. Technol. 10 (1995) 245.
[51] M. Pollock, Philos. Mag. 23 (1971) 519.
[52] V. Lingwal, et al., Bull. Mater. Sci. 26 (6) (2003) 619.
[53] B. Tareev, Phys. Dielectric Mater., Mir Publ., Moscow, 1979 (Chaps. 2 and 3).